https://dx.doi.org/10.21577/0103-5053.20220047

*J. Braz. Chem. Soc.*, Vol. 33, No. 8, 948-957, 2022
©2022 Sociedade Brasileira de Química

**Article**

# Development of Bismuth Oxyhalides for Organic Pollutant Photodegradation and Water Oxidation: Effect of Synthesis Parameter and Halide Species

***Gabriel K. Macedo,[a] Eduardo Henrique Dias,[a,b] Caue Ribeiro[b] and Osmando F. Lopes[*,c]***

[a]*Instituto de Química de São Carlos, Universidade de São Paulo, Av. Trabalhador São Carlense, 400, 13560-970 São Carlos-SP, Brazil*

[b]*Embrapa Instrumentação, Rua XV de Novembro, 1452, 13560-240 São Carlos-SP, Brazil*

[c]*Laboratório de Fotoquímica e Ciência dos Materiais (LAFOT-CM), Instituto de Química, Universidade Federal de Uberlândia (IQUFU), Av. João Naves de Ávila, 2121, Bairro Santa Mônica, 38400-902 Uberlândia-MG, Brazil*

The development of visible-light active photocatalysts is vital to harvest the solar irradiation and build efficient photoelectrochemical devices. Bismuth oxyhalide (BiOCl, BiOBr and BiOI) materials stand out due to their remarkable properties, e.g., the band gap energy can be tuned from 1.9 to 3.4 eV depends on the halide employed. However, the hydrothermal synthesis of this material class was not properly investigated and compared. Then, we evaluated the effect of the hydrothermal treatment in the BiOX's structural, electronic, morphological and textural properties and the relationship with their photocatalytic performance. Methylene blue (MB) dye was used as probe for photocatalytic performance evaluation under ultraviolet (UV) and visible (Vis) radiation. BiOCl and BiOBr samples showed a good photoactivity under both UV and visible radiation, on other hand the BiOI samples was not active, likely due to the fast charge recombination. BiOCl and BiOBr samples exhibit a favorably interaction with MB dye, because their surfaces are negatively charged. BiOCl samples were able to promote around 40 and 80% of the MB dye degradation under visible and UV radiation, respectively. The samples were also employed as photoanode for $O_2$ evolution, BiOI sample exhibited the best performance, due to the synergistic effect of photocatalysis and electrocatalysis.

**Keywords:** BiOX (X = Cl, Br, I), hydrothermal treatment, photocatalysis, organic pollutant photodegradation, $O_2$ evolution

## Introduction

The water contamination by organic pollutants and the emission of greenhouse gas can seriously affect human health and contribute to the climate change.[1,2] Therefore, it is necessary the development of efficient treatment technologies for the removal of these compounds from wastewater and the production of a clean and sustainable fuel (water oxidation).[3,4] Heterogeneous photocatalysis have attracted great interest for this purpose because this process can be powered by solar irradiation.[5] $TiO_2$ and ZnO are the benchmarks photocatalysts to promote the organic pollutant degradation and water oxidation.[6-8]

However, $TiO_2$ and ZnO exhibit a wide band gap (ca. 3.2 eV) that limits its applications and practical efficiency under solar radiation, since less than 5% of solar irradiation is capable to activate $TiO_2$.[6-8] Therefore, several groups have been dedicated to find alternatives to decrease the semiconductor's band gap, such as doping,[9] heterojunction[2] and sensitization.[10,11] On the other hand, the development of semiconductors able to be activated by solar irradiation with high performance is highly required.[12,13]

In this sense, the bismuth oxyhalides (BiOX, X = Cl, Br, I) belong to a group of materials that stands out due to their low band gap range of 3.2 to 1.9 eV, which allows your activation by visible irradiation ($\lambda$ > 440 nm).[14-18] Additionally, they present a suitable valence and conduction band positions for both organic pollutant photodegradation and water oxidation ($O_2$ evolution). Therefore, this material class present a great potential for photocatalytic and

---

*e-mail: osmando_iq@hotmail.com

Editor handled this article: Rodrigo A. A. Muñoz (Associate)

photoelectrocatalytic purposes.[15,19-21] However, to date this material class was poorly investigated, specially the effect of the synthesis parameter and the halide species on their photocatalytic performance.[22] Additionally, it is necessary to develop simple, facile and effective low-temperature method to synthesize bismuth oxyhalides and to investigate the effect of synthesis parameter on the materials properties.[23]

In the present work, we aimed to develop the synthesis method to obtain the bismuth oxyhalides. We evaluated the effect of hydrothermal treatment and the halide species (Cl, Br and I) in the bismuth oxyhalides physical-chemical properties and also in the photocatalytic performance for both organic pollutant degradation and water oxidation. The photocatalytic performance of the samples was evaluated using methylene blue (MB) dye as probe, the samples were also investigated as photoanode to promote the $O_2$ evolution, finally the photodegradation mechanism was described.

## Experimental

### Materials synthesis

Bismuth oxyhalides were prepared by a typical synthesis[14] where 0.7 g of $Bi(NO_3)_3.5H_2O$ (Vetec®, Duque de Caxias-RJ, Brazil) was added to 35 mL of water and subsequently 3 mL of acetic acid (Synth®, Diadema, SP, Brazil) was added to this mixture and stirred vigorously to completion dissolution of the precursor. The respective potassium halide, KX, X = Cl, Br and I (Synth®, Diadema, SP, Brazil) was added to the previous solution in the 1:1 Bi:X molar ratio, then the solutions were treated at room temperature or hydrothermally at 160 °C for 12 h under vigorous stirring. Then, the samples were separated and washed three times with distilled water by centrifugation, to withdrawn impurities.

### Samples characterization

The structural properties of the obtained samples were analyzed by X-ray diffraction (XRD) on a Shimadzu diffractometer (Kyoto, Japan) operating with Cu K$\alpha$ radiation generated at 30 kV and 30 mA filament current. The scan rate of 1° *per* min was applied to record the patterns in the range of 10-60°. The Raman scattering spectra were performed on an FT-Raman spectrometer, Bruker RAM II with Ge detector (Billerica, Massachusetts, USA), equipped with a Nd:YAG laser with wavelength centered at 1064 nm to study the short-range structure of materials. Fourier transform infrared spectroscopy (FTIR) was carried out in a spectrometer, Vertex 70, Bruker (Billerica, Massachusetts, USA) to estimate the surface groups of the materials. The BiOX nanoparticle size were estimated by dynamic light scattering (DLS), using a Malvern Zetasizer Nano ZS instrument (Malvern, Worcestershire, United Kingdom). This system employs dynamic light scattering to measure the diffusion of particles moving under Brownian motion. The same equipment was used to evaluate the charge and ability to form colloidal suspensions measuring the zeta potential of the materials at the same pH of MB dye solution. UV-Visible diffuse reflectance spectroscopy (DRS) was performed on a Shimadzu UV-2600 spectrometer (Kyoto, Japan) in full reflection mode with integration cell (ISR-2600 plus) with a scan interval of 200-800 nm, to estimate the band gap of the samples. The morphology of the samples was evaluated using the scanning electron microscopy (SEM-FEG) in a JEOL JSM 6701F equipment (Tokyo, Japan). The specific surface area of the samples was estimated by $N_2$ physisorption analysis at 77 K in the Micrometrics ASAP 2000 equipment (Norcross, Georgia, USA) applying BET (Brunauer-Emmett-Teller) model. Prior to the analyses, the samples were pre-treated (degasification) by heating at 80 °C under vacuum until reaching a degassing pressure lower than 10 µmHg.

### Evaluation of photocatalytic and photoeletrocatalytic performance

The photocatalytic activity of the as-synthesized samples was evaluated by degradation of the methylene blue dye (Sigma-Aldrich, Saint Louis, Missouri, USA). The reason to use methylene blue as probe to analyze the BiOX's materials photoactivity was included in the Supplementary Information (SI) section. The photodegradation tests were carried out under both visible and UV radiation. These experiments were conducted in a photo-reactor at 18 °C, with visible radiation (Munich, Germany, Osram, 15 W, maximum intensity at 440 nm) and UV radiation sources (Eindhoven, Netherlands, Philips TUV, 15 W, maximum intensity at 254 nm). The spectra of the lamps were included in the SI section (Figure S1). It can be observed that visible lamp exhibits a maximum intensity from 400 to 600 nm, while the UV lamp exhibits a maximum intensity around 254 nm. The photocatalytic performance of the as-synthesized samples was performed by dispersion of 10 mg of photocatalyst in 20 mL of the MB dye aqueous solution (5.0 mg $L^{-1}$). This suspension was placed in the photoreactor under continuous stirring. The MB dye concentration was monitored by its maximum absorption peak at 665 nm at regular intervals in a UV-Vis (Kyoto, Japan, Shimadzu-

1601PC) spectrophotometer in the absorption mode. The samples with the organic pollutant were kept in the dark during 12 h prior to the photocatalytic tests to achieve the equilibrium of the adsorption-desorption processes. All BiOX-samples presented a negligible adsorption of MB dye.

Photoelectrochemical measurements were carried out using a potentiostat Metrohm Autolab PGSTAT204 (Utrecht, Netherlands) in a homemade three-electrode photoelectrochemical cell using 0.1 mol L$^{-1}$ $Na_2SO_4$ (Sigma-Aldrich, Saint Louis, Missouri, USA) as the electrolyte, Pt wire (Metrohm, Utrecht, Netherlands) as a counter electrode, a home-made Ag/AgCl (3 mol L$^{-1}$ NaCl) as a reference electrode and a photoanode as working electrode. The photoanode with an irradiation area of 1 cm$^2$ were prepared by the deposition of each sample on fluoride-doped tin oxide (FTO)-coated glasses (Sigma-Aldrich, 8 Ω s$^{-1}$, Saint Louis, Missouri, USA) by drop casting method. The film was prepared mixing 10 mg of sample, 2 mL of Milli-Q water, 20 µL of PEDOT:PSS (poly(3,4-ethylenedioxythiophene)-poly(styrenesulfonate) a conductive binder, Sigma-Aldrich, Saint Louis, Missouri, USA), then the dispersion was kept in an ultrasound bath (Analitica®, São Paulo, SP, Brazil) for 10 min. After homogenous dispersion 100 µL of the solution (divided into two applications of 50 µL) were dropped over FTO-glass heated by a heating plate at 80 °C. The linear sweep voltammetry (LSV) measurements were recorded in the dark and under front illumination with a scan rate of 25 mV s$^{-1}$. A halogen lamp (100 W) was used as the light source. The sample with the best performance was also investigated applying 1.3 V *vs.* Ag/AgCl with chopped light and compared with $BiVO_4$.

## Results and Discussion

### Powder microstructural characterization

The XRD patterns of the BiOCl, BiOBr and BiOI samples (Figures 1a-1c) prepared by hydrothermal treatment (160 °C) and at room temperature demonstrated that both conditions resulted in tetragonal crystalline phase of P4/mmm symmetry, PDF (Powder Diffraction File) No. 73-2060, 78-0348 and 85-0863, respectively.[24-26] Bismuth oxyhalides is a layered structure made up of [X–Bi–O–Bi–X] slabs (X = Cl, Br and I) stacked together by van der Waals interactions to form a tetragonal matlockite structure (a characteristic basal peak around 10° can be observed for all samples), each bismuth center is surrounded by four oxygen atoms and four halogen atoms, giving rise to an asymmetric decahedral symmetry. The crystalline structure of BiOX materials can be checked elsewhere in details.[27-32] It was observed that the synthesis method employed was efficient to obtain the pure bismuth oxyhalides. The change at temperature treatment caused only a difference in the preferential orientation growth along the [001] direction. It can be observed that the BiOX samples obtained at 25 °C exhibited a stronger (001) peaks intensity than the samples obtained at 160 °C, as can be observed by the ratio of (001)/(102) peaks intensity

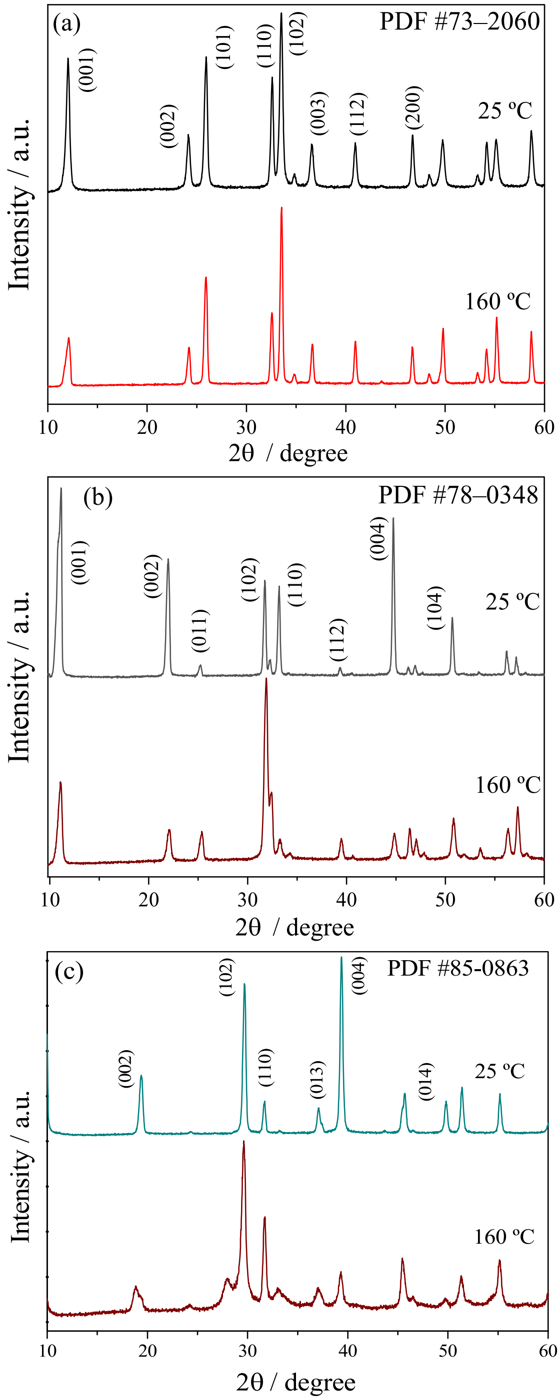

**Figure 1.** XRD patterns of the (a) BiOCl, (b) BiOBr and (c) BiOI samples obtained at room temperature and 160 °C by hydrothermal treatment.

(Table S1, SI section). It can be related to different particle's morphologies due to different synthesis conditions. Despite the differences at preferential orientation, the samples obtained in different temperatures presented very similar peaks broadening, it means that the temperature treatment does not affect the samples crystallite size. It was demonstrated that the proposed method was efficient to obtain the respective crystalline materials without the presence of impurities.

BiOX samples were also characterized by Raman analysis to investigate their structure and confirm the XRD results (Figures 2a-2c). BiOCl showed peaks at 64, 147, 202 and 401 cm$^{-1}$ (Figure 2a), which can be related to four different Raman modes of BiOCl in the tetragonal crystalline phase.[33-35] The peak at 64 cm$^{-1}$ can be assigned to the external stretch mode (A$_{1g}$) from Bi–Cl bond, the peaks at 147 and 202 cm$^{-1}$ can be related to the internal stretch from Bi–Cl bond with symmetry A$_{1g}$ and E$_{1g}$, respectively.[33,35] Additionally, the broad band at 400 cm$^{-1}$ can be related to the motion of the oxygen atoms.[35,36] BiOBr samples exhibited peaks at 60, 92, 114, 163 and 391 cm$^{-1}$ (Figure 2b). The first four peaks can be attributed to the Bi–Br stretching modes, which the peaks at 60 and 114 cm$^{-1}$ are related to external and internal stretch Bi–Br with A$_{1g}$ symmetry, respectively. The peaks at 92 and 163 cm$^{-1}$ can be ascribed to the E$_{1g}$ external and E$_{2g}$ internal Bi–Br stretching mode, respectively.[37,38] The broad band at 391 cm$^{-1}$ can be related with the motion of the oxygen atoms.[37-39] BiOI samples exhibited bands at 90 and 152 cm$^{-1}$ (Figure 2c) ascribed to the internal stretch A$_{1g}$ and internal stretch mode Eg, respectively.[40,41] Therefore, the Raman analysis confirms the XRD results that the synthesis method was efficient to obtain the BiOX samples without any impurities.

The band gap of the bismuth oxyhalide samples were determined by diffuse reflectance UV-Vis spectroscopy using Tauc equation,[42] Figure 3a and Table 1. It can be observed that the hydrothermal treatment at 160 °C does not affect the band gap energy. BiOCl, BiOBr and BiOI samples presented band gap value of 3.4, 2.7 and 1.9 eV, respectively, in close agreement with the literature.[19] The DRS spectra of BiOCl, BiOBr and BiOI materials (Figure 3b) show an absorbance threshold at about 370, 460 and 650 nm, respectively, in agreement with the literature.[43] Then, it can be confirmed that BiOBr and BiOI can be activated by both visible and UV lamp, while the BiOCl can be activated only by UV lamp.[44-46] We observed experimentally that the BiOX's band gaps decrease with the increase of atomic number of the halide (Cl, Br, and I elements). Several authors demonstrated by first-principles calculations that the BiOX's valence band originates principally from the O 2p and X *n*p orbitals (where, *n* is the principal quantum number of the respective halide) while the conduction band is mainly formed by the Bi 6p orbital. As X gets larger the interatomic overlap of X *n*p and O 2p also increases, then the contribution of X *n*s states for the valence band increases, then the valence band position is shifted and the band gap is decreased as the X gets larger.[47-50]

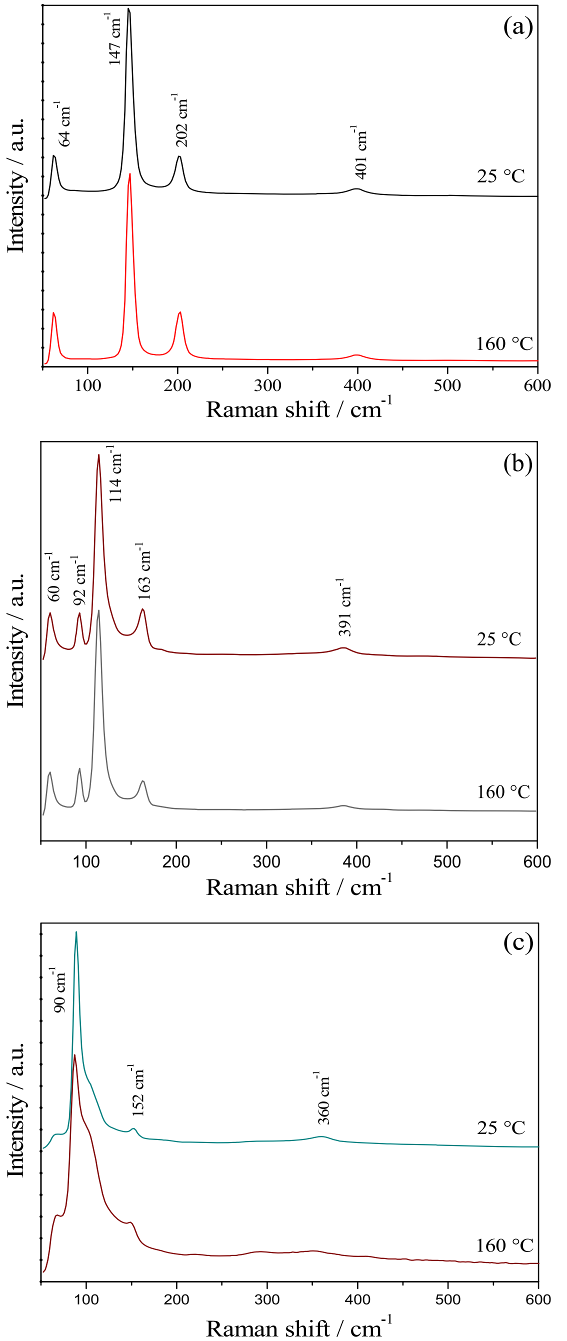

**Figure 2.** Raman spectra of the (a) BiOCl, (b) BiOBr and (c) BiOI samples obtained at 25 and 160 °C.

The samples' zeta potential value was determined at the same pH of the MB solution (pH ca. 6) (Table 1). It

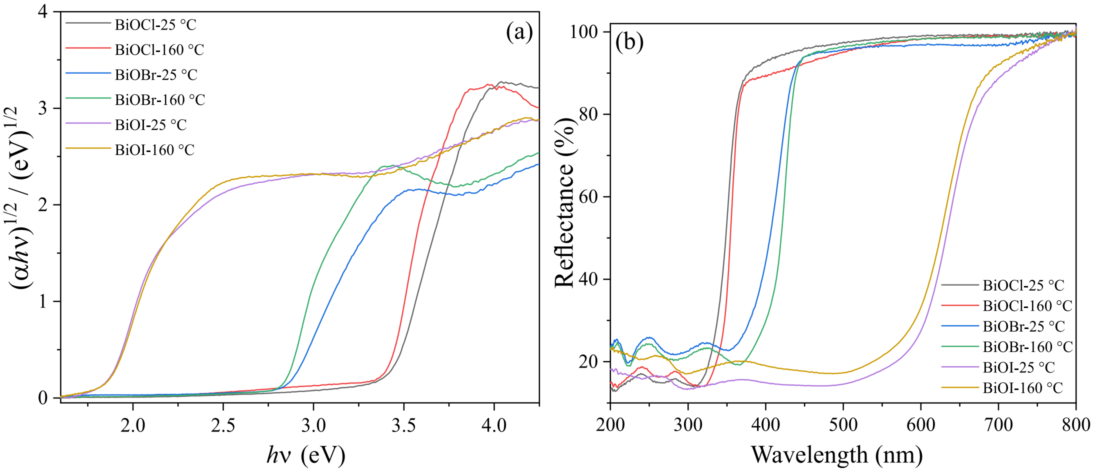

**Figure 3.** (a) Plots of $(\alpha h\nu)^{1/2}$ *vs.* photon energy (hν) obtained by Tauc equation from DRS spectra of the BiOX samples (X = Cl, Br and I). (b) Diffuse reflectance spectra of the BiOX samples.

can be observed that BiOCl-25 °C sample exhibited a zeta potential higher than 30 mV, it means that this sample nanoparticles can form a stable colloidal suspension.[51] The increase at the synthesis temperature to 160 °C decreased the zeta potential value to around 18 mV, likely because the increase at the temperature removed some surface charged groups. Both BiOBr samples exhibited similar value of zeta potential and can form also stable colloidal suspensions. BiOI samples presented the lowest zeta potential value, so they are expected to agglomerate and precipitate during the photocatalysis application if applied as free-standing powder.

**Table 1.** Zeta potential (ζ) at pH 6, specific surface area (SSA) and band gap energy of BiOX samples

| Sample | ζ / mV | SSA / ($m^2 g^{-1}$) | Band gap / eV |
|---|---|---|---|
| BiOCl-25 °C | −32.6 | 1.1 | 3.4 |
| BiOCl-160 °C | −18.0 | [a] | 3.4 |
| BiOBr-25 °C | −25.5 | 0.3 | 2.8 |
| BiOBr-160 °C | −24.9 | [a] | 2.7 |
| BiOI-25 °C | −3.0 | [a] | 1.9 |
| BiOI-160 °C | 7.9 | 46.4 | 1.9 |

[a] These samples presented a specific surface area lower than the quantification limit of the $N_2$ physisorption measurement.

SEM images were obtained to study the effect of synthesis temperature at BiOX's morphology, Figure 4. BiOCl obtained at room temperature exhibited micrometric particles with a conventional plate-like morphology.[35] BiOCl obtained at 160 °C exhibited similar morphology, however the particle size was much lower than the sample obtained at room temperature, it means that during the hydrothermal process some redissolution and reprecipitation happened. This result is in agreement with the DLS results (Figure S2, SI section). BiOBr obtained at room temperature presented micrometric and agglomerated sheet-like morphology, in agreement with the literature.[52] The BiOBr obtained by the hydrothermal treatment at 160 °C presented a completely different morphology, i.e., dense microplates. These results are not in agreement with the DLS results, maybe due to the great difference in the morphology of both samples. The BiOI obtained at room temperature showed a large variation in the size of the particles, most of them with several micrometers and some of them in the nanometric scale, all of them with the same plate-like morphology. It is in agreement with the DLS results.[53] However, the BiOI obtained at 160 °C presented particles with the same size range, however the surface of these particles is rougher than the sample obtained at 25 °C. This morphology behavior agrees with the highest specific surface area of BiOI-160 °C (Table 1). On the other hand, both BiOCl and BiOBr samples exhibited very small SSA values probably due to their large and dense particles as observed by SEM analysis.

### Photocatalytic performance evaluation

The performance of BiOX samples was evaluated by MB photodegradation carried out under visible irradiation, Figure 5. BiOCl and BiOBr were active for MB dye photodegradation under visible radiation. On the other hand, both BiOI samples presented an insignificant photocatalytic performance, likely due to its narrow band gap (Figure 3 and Table 1) that results in a valence band position with a lower capacity to promote the oxidation, then it is unable to promote the $^{\bullet}OH$ radical formation.[19,54-56] Under visible radiation, it was observed that the samples of BiOCl and BiOBr obtained at room temperature presented higher activity than those hydrothermally treated at 160 °C.

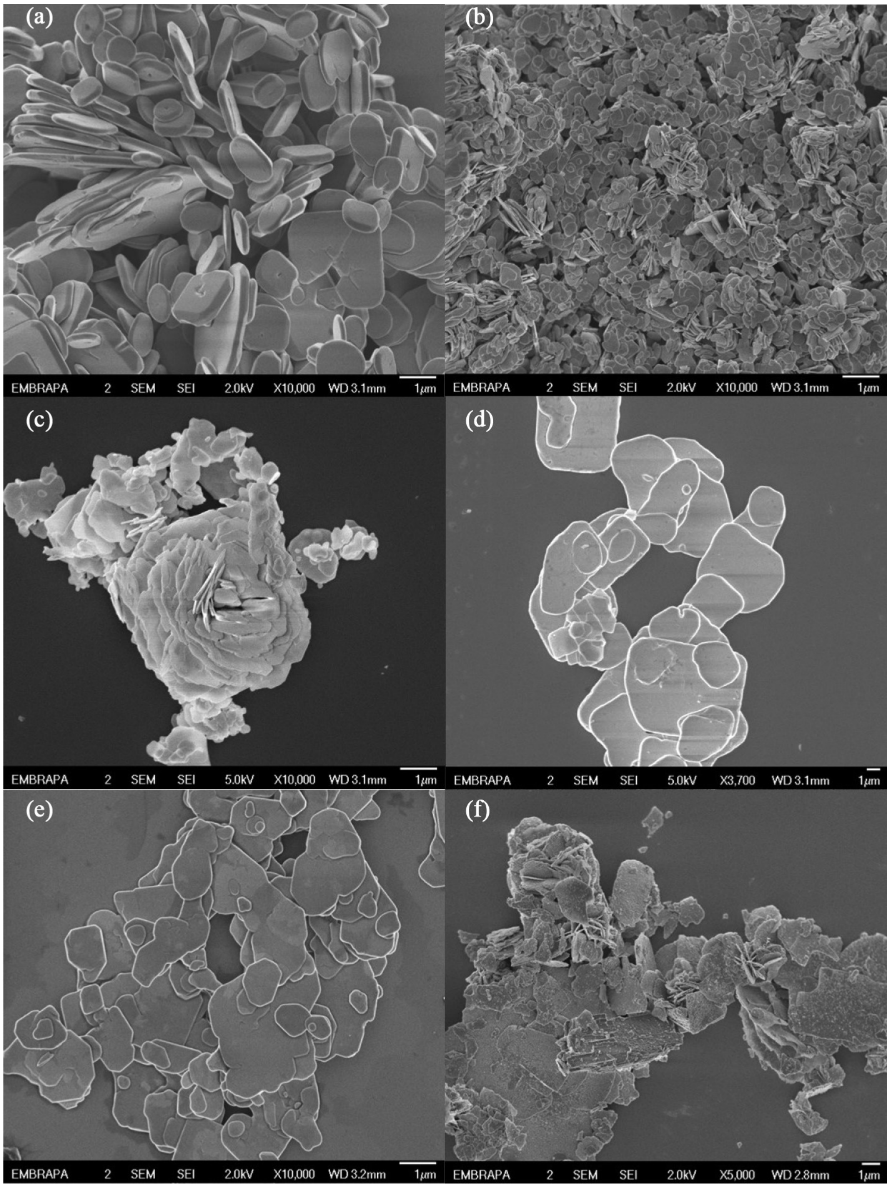

**Figure 4.** SEM images of the (a) BiOCl-25 °C, (b) BiOCl-160 °C, (c) BiOBr-25 °C (d) BiOBr-160 °C, (e) BiOI-25 °C and (f) BiOI-160 °C.

In the BiOBr sample this effect may be related to the increase of the particle size and decrease in the specific surface area caused by the hydrothermal treatment as shown by the SEM images (Figure 4) and by SSA values in Table 1. The hydrothermal treatment in BiOCl resulted in a less charged surface as observed by zeta potential measurement (Table 1) that decreases the interaction with the MB dye, a cationic dye,[57] decreasing the MB degradation rate on the surface of the semiconductor. We used $BiVO_4$ sample as a reference to compare our results, since $BiVO_4$ is considered a benchmark material for organic pollutant photodegradation under visible radiation.[44-46,58] Our best material presented a photoactivity very close to the reference material ($BiVO_4$), then, we can confirm that our materials exhibit a good photoactivity.[45,46,58]

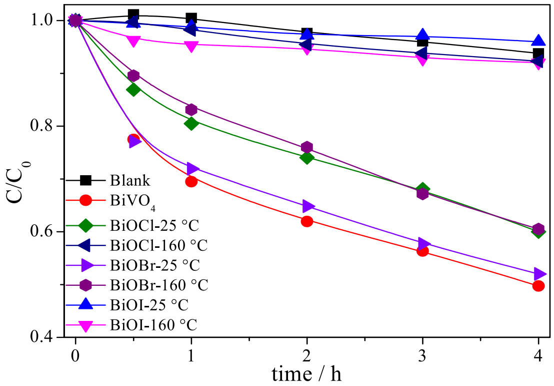

**Figure 5.** MB dye photodegradation catalyzed by the BiOX (X = Cl, Br, I) and $BiVO_4$ samples as a function of the exposure time under visible irradiation. Conditions: 18 °C, 10 mg of BiOX samples, 10 mg $L^{-1}$ of MB dye.

BiOCl-25 °C was able to promote about 40% of MB dye discoloration, likely due to the photosensitization mechanism, in this process a molecule adsorbed on the surface of the catalyst is excited by the visible light and its excited electron is transferred from molecule's lowest unoccupied molecular orbital (LUMO) to the semiconductor's conduction band, causing the 1st step of the molecule oxidation.[59-61] The transferred electron can react with the $O_2$ molecule forming the radical superoxide ($O_2^{-\bullet}$), which can promote the further oxidation of the MB dye.[61-64]

As can be observed in Figure 6 under UV irradiation BiOCl and BiOBr samples were photoactive in the MB dye degradation and once again for the same reason the BiOI samples were inactive. BiOCl sample obtained at room temperature exhibited the highest MB dye degradation, because under UV irradiation the BiOCl can be activated and then generate the radical species that can trigger the MB dye oxidation. In this sense, BiOCl can promote the MB dye degradation by two different mechanisms at the same time, photocatalytic (electron/hole generation) and photosensitization process. BiOCl obtained at 160 °C presented a lower performance due to its lower interaction with the MB dye caused by the less negatively charged surface. BiOBr samples also presented a good MB dye degradation, with the sample obtained at 160 °C presenting a higher performance than the sample obtained at room temperature. Based in a previous work[65] from our group we can propose the MB dye oxidation mechanism under UV radiation (Figure S3, SI section). In the first steps, $^{\bullet}OH$ radical promote the successive hydroxylation in the aromatic ring of the MB molecule. Then, one or more methyl substituents from the amine groups of MB are lost, forming the azure B, azure A, and azure C species, respectively.[66,67] Finally, the attack of actives species generated from the BiOX samples to the azure species promote the cleavage of the aromatic ring.[65] It confirms that MB dye molecules were broken down by the photocatalytic process, which was a strong indication of the occurrence of a mineralization process.

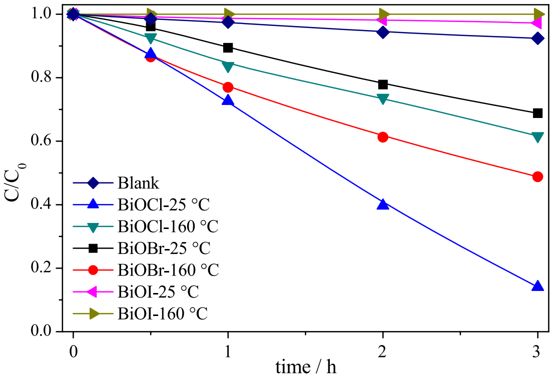

**Figure 6.** MB dye photodegradation test catalyzed by the BiOX samples (X = Cl, Br, I) as a function of the exposure time under UV irradiation. Conditions: 18 °C, 10 mg of BiOX samples, 10 mg $L^{-1}$ of MB dye.

In order to test the reproducibility of the photocatalytic tests, the experiments were performed in triplicate, and the first-order rate constant and the respective standard deviation was calculated for each condition (Table S2, SI section). We can confirm that the results are well reproducible and the photoactivity order is the same when the standard deviation was included. The coefficient of determination ($R^2$ values) higher than 0.95 confirm that the pollutant photodegradation follows a first-order mechanism.

Under visible and UV radiation, the BiOX samples obtained at room temperature presented a higher activity for MB dye photodegradation than the samples obtained under hydrothermal conditions at 160 °C. Then, BiOX samples obtained at room temperature were further investigated as photoanode for water oxidation reaction (i.e., $O_2$ evolution reaction). All electrodes based on BiOX samples were characterized by LSV curves under dark and UV-Vis irradiation condition (Figure 7). It was verified that all samples were prompt in generating photocurrent, demonstrating effective charge transfer and successfully electron collection for the samples within the photoelectrochemical cell. Additionally, it was also observed that all samples decreased the onset potential (ca. 10-20 mV) for $O_2$ evolution reaction (Figure 7).

The LSV curves illuminated showed that BiOCl sample presented the highest performance for $O_2$ evolution (Figure 8a), in agreement with the literature and the MB dye photodegradation experiments. BiOI sample presented the lowest onset potential (ca. 1.3 V *vs.* Ag/AgCl), then this sample was also compared with $BiVO_4$ (a reference material for $O_2$ evolution reaction).[68,69] Then, a chronoamperometry experiment using both BiOI and $BiVO_4$ applying 1.3 V *vs.* Ag/AgCl upon chopped irradiation was performed (Figure 8b). It was confirmed that BiOI exhibited a good performance as photoanode for $O_2$ evolution with a current density about 35 μA $cm^{-2}$, while $BiVO_4$ presented a photocurrent density about 20 μA $cm^{-2}$ in the same potential. Then, the BiOI sample presented a higher activity than the benchmark material ($BiVO_4$).

Turnover frequency (TOF) is an important parameter to evaluate the intrinsic activity of the samples, it was calculated as:

$$\mathrm{TOF} = (\mathrm{j} \times \mathrm{N_A})/(\mathrm{F} \times \mathrm{n} \times \Gamma) \qquad (1)$$

where, j, $N_A$, F, n, and Γ represent current density, the Avogadro constant, the Faraday constant, the number of electrons transferred to generate one molecule of the product, and the surface concentration or exact number

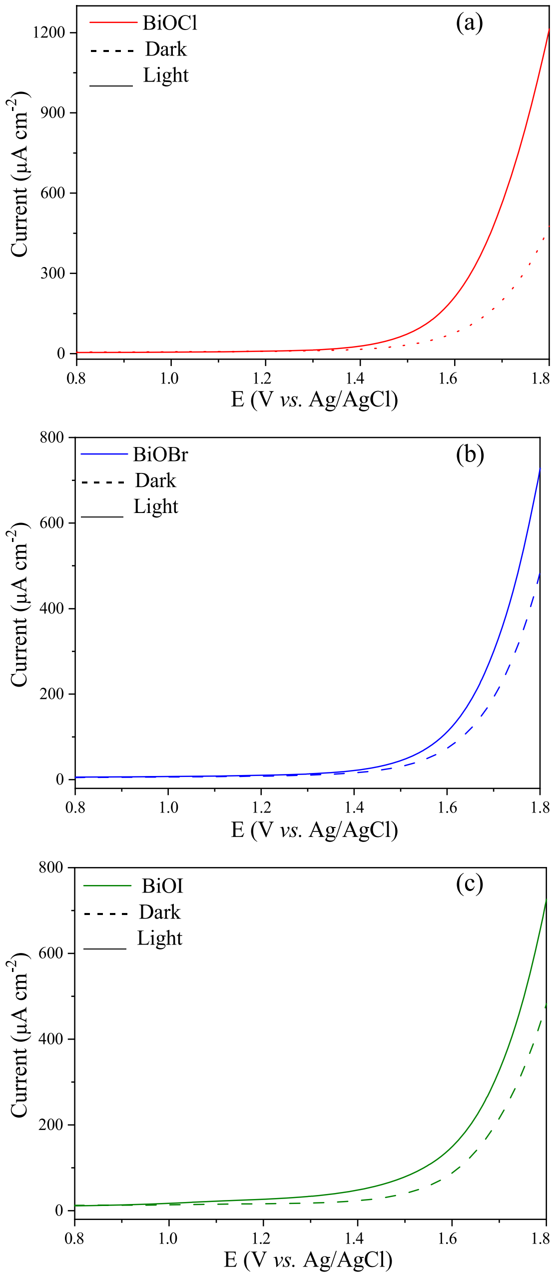

**Figure 7.** Comparison of linear sweep voltammetry curves under dark and illuminated conditions in aqueous 0.1 mol L$^{-1}$ $Na_2SO_4$ solution (pH 6) for (a) BiOCl, (b) BiOBr and (c) BiOI samples deposited on FTO by drop-casting.

of active sites catalyzing the reaction (m$^{-2}$), respectively.

The Table S3 (SI section) exhibits the TOF value of the BiOX samples measured at 1.6 V *vs.* Ag/AgCl. It can be observed that BiOI-25 °C presented a turnover frequency higher than the other samples and its TOF value is very close to the benchmark catalysts applied for water oxidation. Zhou *et al.*[70] prepared electrodes of Ni-based hydroxides hierarchical nanoarrays with an optimized TOF value of 0.17 s$^{-1}$. Meyer and co-workers[71] observed that a molecular catalyst Ru-based presented a TOF value of 0.18 s$^{-1}$. It is indicative of the high performance of the BiOX electrodes. On the other hand, this kind of comparison is not so reliable, because those electrodes have composition and properties completely different and the TOF value were estimated using different strategies.

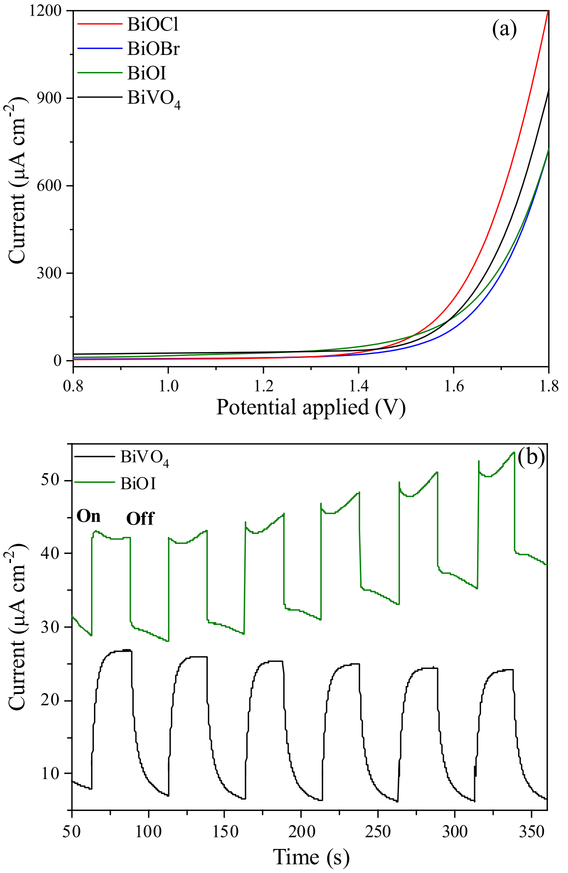

**Figure 8**. (a) Linear sweep voltammetry curves in aqueous 0.1 M $Na_2SO_4$ solution (pH 6) under UV-Vis irradiation for BiOX-25 ºC and $BiVO_4$ samples deposited on FTO by drop-casting. (b) Photocurrent time dependence applying 1.3 V *vs.* Ag/AgCl of BiOI and $BiVO_4$ upon chopped irradiation.

## Conclusions

The synthesis method was efficient to obtain the BiOX samples with tunable microstructural properties. The BiOX (Cl and Br) samples showed a good photocatalytic activity on the MB dye degradation under both UV and visible radiation, on other hand the BiOI samples do not showed photocatalytic activity. The BiOCl samples was able to degrade around 40% of the MB dye due to the photosensitization process under visible radiation. The samples of BiOCl and BiOBr are negatively charged and exhibited a good interaction with MB molecules (cationic dye). This interaction may be responsible to increase the photocatalytic activity, since in a mechanism of direct charge transfer with the dye and in a photosensitization process it is necessary the direct contact between the molecule dye and catalyst surface to provide the conditions for charge transfer. Finally, all BiOX samples were active as photoanode for $O_2$, where BiOI sample exhibited the best performance, because the synergistic effect of photoelectrochemical process enhanced the electron/hole separation and improved its oxidation ability.

## Supplementary Information

Supplementary information is available free of charge at http://jbcs.sbq.org.br as PDF file.

## Acknowledgments

The authors acknowledge FAPEMIG (Minas Gerais Research Foundation, grant: APQ-00282-21) and CNPq (Brazilian National Council for Scientific and Technological Development, grant No. 407497/2018-8) for the financial support, and FAPESP (São Paulo Research Foundation) for the financial support (grant No. 2018/01258-5) scholarship (grant No. 2019/10689-2). O. F. Lopes also acknowledges Alexander von Humboldt Foundation and CAPES by Post-Doc Research Fellowship (CAPES/Humboldt Agreement-Process 88881.368050/2019-01, Finance code 001). The authors are also grateful to the Ministry of Science, Technology, and Innovation (SisNANO Program - National System of Laboratories in Nanotechnology).

## References

1. da Silva, G. T. S. T.; Lopes, O. F.; Dias, E. H.; Torres, J. A.; Nogueira, A. E.; Faustino, L. A.; Prado, F. S.; Patrocínio, A. O. T.; Ribeiro, C.; *Quim Nova* **2021**, *44*, 963.
2. Bueno, R. T.; Lopes, O. F.; Carvalho, K. T. G.; Ribeiro, C.; Mourão, H. A. J. L.; *Quim. Nova* **2019**, *42*, 661.
3. Nunes, B. N.; Lopes, O. F.; Patrocinio, A. O. T.; Bahnemann, D. W.; *Catalysts* **2020**, *10*, 126.
4. Tekin, G.; Ersöz, G.; Atalay, S.; *J. Environ. Manage.* **2018**, *228*, 441.
5. You, J.; Guo, Y.; Guo, R.; Liu, X.; *Chem. Eng. J.* **2019**, *373*, 624.
6. Likodimos, V.; *Appl. Catal., B* **2018**, *230*, 269.
7. Sun, H.; Wang, S.; Ang, H. M.; Tadé, M. O.; Li, Q.; *Chem. Eng. J.* **2010**, *162*, 437.
8. Rehman, S.; Ullah, R.; Butt, A. M.; Gohar, N. D.; *J. Hazard. Mater.* **2009**, *170*, 560.
9. Medhi, R.; Marquez, M. D.; Lee, T. R.; *ACS Appl. Nano Mater.* **2020**, *3*, 6156.
10. Pelaez, M.; Nolan, N. T.; Pillai, S. C.; Seery, M. K.; Falaras, P.; Kontos, A. G.; Dunlop, P. S. M.; Hamilton, J. W. J.; Byrne, J. A.; O'Shea, K.; Entezari, M. H.; Dionysiou, D. D.; *Appl. Catal., B* **2012**, *125*, 331.
11. Zhang, N.; Wen, L.; Yan, J.; Liu, Y.; *Chem. Pap.* **2020**, *74*, 389.
12. Kumar, S. G.; Devi, L. G.; *J. Phys. Chem. A* **2011**, *115*, 13211.
13. Afonso, R.; Serafim, J. A.; Lucilha, A. C.; Silva, M. R.; Lepre, L. F.; Ando, R. A.; Dall'Antonia, L. H.; *J. Braz. Chem. Soc.* **2014**, *25*, 726.
14. Cao, J.; Xu, B.; Luo, B.; Lin, H.; Chen, S.; *Catal. Commun.* **2011**, *13*, 63.
15. Yao, L.; Yang, H.; Chen, Z.; Qiu, M.; Hu, B.; Wang, X.; *Chemosphere* **2021**, *273*, 128576.
16. Liu, Y.; Yang, B.; He, H.; Yang, S.; Duan, X.; Wang, S.; *Sci. Total Environ.* **2022**, *804*, 150215.
17. Sharma, K.; Dutta, V.; Sharma, S.; Raizada, P.; Hosseini-Bandegharaei, A.; Thakur, P.; Singh, P.; *J. Ind. Eng. Chem.* **2019**, *78*, 1.
18. Hu, X.; Cheng, L.; Li, G.; *Mater. Lett.* **2017**, *203*, 77.
19. Yang, Y.; Zhang, C.; Lai, C.; Zeng, G.; Huang, D.; Cheng, M.; Wang, J.; Chen, F.; Zhou, C.; Xiong, W.; *Adv. Colloid Interface Sci.* **2018**, *254*, 76.
20. Zhang, L.; Wang, W.; Sun, S.; Jiang, D.; Gao, E.; *Appl. Catal., B* **2015**, *162*, 470.
21. Wang, S.-l.; Wang, L.-l.; Ma, W.-h.; Johnson, D. M.; Fang, Y.-F.; Jia, M.-k.; Huang, Y.-p.; *Chem. Eng. J.* **2015**, *259*, 410.
22. Ahmad, I.; Shukrullah, S.; Yasin Naz, M.; Ullah, S.; Ali Assiri, M.; *J. Ind. Eng. Chem.* **2022**, *105*, 1.
23. Wang, Z.; Chen, M.; Huang, D.; Zeng, G.; Xu, P.; Zhou, C.; Lai, C.; Wang, H.; Cheng, M.; Wang, W.; *Chem. Eng. J.* **2019**, *374*, 1025.
24. Gao, K.; Gao, X.; Zhu, W.; Wang, C.; Yan, T.; Fu, F.; Liu, J.; Liang, C.; Li, Q.; *Chem. Eng. J.* **2021**, *406*, 127155.
25. Yuan, Q.; Wei, S.; Hu, T.; Ye, Y.; Cai, Y.; Liu, J.; Li, P.; Liang, C.; *J. Phys. Chem. C* **2021**, *125*, 18630.
26. Kim, W. J.; Pradhan, D.; Min, B. K.; Sohn, Y.; *Appl. Catal., B* **2014**, *147*, 711.
27. Xiong, J.; Cheng, G.; Li, G.; Qin, F.; Chen, R.; *RSC Adv.* **2011**, *1*, 1542.
28. Wei, X.; Akbar, M. U.; Raza, A.; Li, G.; *Nanoscale Adv.* **2021**, *3*, 3353.
29. Lima, G. D. O.; Araujo, T. P.; Lima, J. R. D. O.; Prazeres, G. M. P.; Paschoal, C. W. A.; Longo, E.; Tanaka, A. A.; Maciel, A. P.; Barbosa, D. A. B.; Almeida, M. A. P.; *Bol. Soc. Esp. Ceram. Vidrio* **2021**, *60*, 2.
30. Bhachu, D. S.; Moniz, S. J. A.; Sathasivam, S.; Scanlon, D. O.; Walsh, A.; Bawaked, S. M.; Mokhtar, M.; Obaid, A. Y.; Parkin, I. P.; Tang, J.; Carmalt, C. J.; *Chem. Sci.* **2016**, *7*, 4832.
31. Di, J.; Chen, C.; Yang, S. Z.; Ji, M.; Yan, C.; Gu, K.; Xia, J.; Li, H.; Li, S.; Liu, Z.; *J. Mater. Chem. A* **2017**, *5*, 14144.
32. Li, H.; Li, J.; Ai, Z.; Jia, F.; Zhang, L.; *Angew. Chem., Int. Ed.* **2018**, *130*, 128.

33. Zhou, Y.; Wang, H.; Liu, X.; Zeng, D.; Wang, K.; Zhang, L.; Wang, W.; *Appl. Catal., B* **2021**, *294*, 120265.
34. Tian, Y.; Guo, C. F.; Guo, Y.; Wang, Q.; Liu, Q.; *Appl. Surf. Sci.* **2012**, *258*, 1949.
35. Lei, Y.; Wang, G.; Song, S.; Fan, W.; Zhang, H.; *CrystEngComm* **2009**, *11*, 1857.
36. Lu, J.; Zhou, W.; Zhang, X.; Xiang, G.; *J. Phys. Chem. Lett.* **2020**, *11*, 1038.
37. Ferrer, M. M.; Rodrigues, J. E. F. S.; Almeida, M. A. P.; Moura, F.; Longo, E.; Pizani, P. S.; Sambrano, J. R.; *J. Raman Spectrosc.* **2018**, *49*, 1356.
38. López-Velázquez, K.; Guzmán-Mar, J. L.; Hernández-Ramírez, A.; González-Juárez, E.; Villanueva-Rodríguez, M.; *Mater. Sci. Semicond. Process.* **2021**, *123*, 105499.
39. Zhang, X.; Zhang, Y.; Feng, Z.; Zhao, J.; Yang, Z.; Wang, X.; Wang, W.; *Chem. Eng. J.* **2022**, *428*, 131235.
40. Huang, Y.; Li, H.; Fan, W.; Zhao, F.; Qiu, W.; Ji, H.; Tong, Y.; *ACS Appl. Mater. Interfaces* **2016**, *8*, 27859.
41. Guo, J.; Li, X.; Liang, J.; Yuan, X.; Jiang, L.; Yu, H.; Sun, H.; Zhu, Z.; Ye, S.; Tang, N.; Zhang, J.; *Coord. Chem. Rev.* **2021**, *443*, 214033.
42. Makuła, P.; Pacia, M.; Macyk, W.; *J. Phys. Chem. Lett.* **2018**, *9*, 6814.
43. Natarajan, K.; Bajaj, H. C.; Tayade, R. J.; *J. Ind. Eng. Chem.* **2016**, *34*, 146.
44. Lopes, O. F.; Carvalho, K. T. G.; Avansi, W.; Ribeiro, C.; *J. Phys. Chem. C* **2017**, *121*, 13747.
45. Lopes, O. F.; Carvalho, K. T. G.; Nogueira, A. E.; Avansi, W.; Ribeiro, C.; *Appl. Catal., B* **2016**, *188*, 87.
46. Lopes, O. F.; Carvalho, K. T. G.; Macedo, G. K.; de Mendonça, V. R.; Avansi, W.; Ribeiro, C.; *New J. Chem.* **2015**, *39*, 6231.
47. Barhoumi, M.; Said, M.; *Mater. Sci. Eng., B* **2021**, *264*, 114921.
48. Yin, G. X.; Lv, S. J.; Wang, H. Y.; *Solid State Commun.* **2021**, *336*, 114419.
49. Zhao, L.; Zhang, X.; Fan, C.; Liang, Z.; Han, P.; *Phys. B* **2012**, *407*, 3364.
50. Zhang, K. L.; Liu, C. M.; Huang, F. Q.; Zheng, C.; Wang, W. D.; *Appl. Catal., B* **2006**, *68*, 125.
51. Malta, J. O.; Oliveira, L. V. S.; Ueki, M. M.; Barreto, L. S.; *Powder Technol.* **2021**, *383*, 43.
52. Imam, S. S.; Adnan, R.; Mohd Kaus, N. H.; *J. Environ. Chem. Eng.* **2021**, *9*, 105404.
53. Jiang, Y.-R.; Chou, S.-Y.; Chang, J.-L.; Huang, S.-T.; Lin, H.-P.; Chen, C.-C.; *RSC Adv.* **2015**, *5*, 30851.
54. Jahurul Islam, M.; Amaranatha Reddy, D.; Han, N. S.; Choi, J.; Song, J. K.; Kim, T. K.; *Phys. Chem. Chem. Phys.* **2016**, *18*, 24984.
55. Huang, J.; Zheng, X.; Liu, Y.; Wang, F.; Li, D.; Liu, H.; Li, R.; Chen, T.; Lv, W.; Liu, G.; *J. Hazard. Mater.* **2021**, *412*, 125147.
56. Islam, M. J.; Reddy, D. A.; Ma, R.; Kim, Y.; Kim, T. K.; *Solid State Sci.* **2016**, *61*, 32.
57. Mourão, H. A. J. L.; Lopes, O. F.; Ribeiro, C.; Mastelaro, V. R.; *Mater. Sci. Semicond. Process.* **2015**, *30*, 651.
58. Lopes, O. F.; Carvalho, K. T. G.; Avansi, W.; Milori, D. M. B.; Ribeiro, C.; *RSC Adv.* **2018**, *8*, 10889.
59. Lopes, O. F.; Paris, E. C.; Ribeiro, C.; *Appl. Catal., B* **2014**, *144*, 800.
60. Zhang, L.; Niu, C. G.; Zhao, X. F.; Liang, C.; Guo, H.; Zeng, G. M.; *ACS Appl. Mater. Interfaces* **2018**, *10*, 39723.
61. Chou, Y. C.; Lin, Y. Y.; Lu, C. S.; Liu, F. Y.; Lin, J. H.; Chen, F. H.; Chen, C. C.; Wu, W. T.; *J. Environ. Manage.* **2021**, *297*, 1.
62. Bárdos, E.; Márta, V.; Baia, L.; Todea, M.; Kovács, G.; Baán, K.; Garg, S.; Pap, Z.; Hernadi, K.; *Appl. Surf. Sci.* **2020**, *518*, 146184.
63. Li, Z.; Huang, G.; Liu, K.; Tang, X.; Peng, Q.; Huang, J.; Ao, M.; Zhang, G.; *J. Cleaner Prod.* **2020**, *272*, 122892.
64. Siao, C. W.; Chen, H. L.; Chen, L. W.; Chang, J. L.; Yeh, T. W.; Chen, C. C.; *J. Colloid Interface Sci.* **2018**, *526*, 322.
65. da Silva, G. T. S. T.; Carvalho, K. T. G.; Lopes, O. F.; Gomes, E. S.; Malagutti, A. R.; Mastelaro, V. R.; Ribeiro, C.; Mourao, H. A. J. L.; *ChemCatChem* **2017**, *9*, 3795.
66. Petzer, A.; Harvey, B. H.; Wegener, G.; Petzer, J. P.; *Toxicol. Appl. Pharmacol.* **2012**, *258*, 403.
67. Houas, A; Lachheb, H.; Ksibi, M.; Elaloui, E.; Guillard, C.; Herrmann, J.-M.; *Appl. Catal., B* **2001**, *31*, 145.
68. Zhao, F.; Li, N.; Wu, Y.; Wen, X.; Zhao, Q.; Liu, G.; Li, J.; *Int. J. Hydrogen Energy* **2020**, *45*, 31902.
69. Wang, S.; Chen, P.; Yun, J. H.; Hu, Y.; Wang, L.; *Angew. Chem., Int. Ed.* **2017**, *56*, 8500.
70. Zhou, T.; Cao, Z.; Zhang, P.; Ma, H.; Gao, Z.; Wang, H.; Lu, Y.; He, J.; Zhao, Y.; *Sci. Rep.* **2017**, *7*, 46154.
71. Concepcion, J. J.; Binstead, R. A.; Alibabaei, L.; Meyer, T. J.; *Inorg. Chem.* **2013**, *52*, 10744.

*Submitted: October 22, 2021*
*Published online: March 14, 2022*